

Development of complex patterns of anthropogenic uplift and subsidence in the Delaware Basin of West Texas and southeast New Mexico, USA

Peter Hennings^{a,*}, Scott Staniewicz^b, Katie Smye^a, Jingyi Chen^b, Elizabeth Horne^a, Jean-Philippe Nicot^a, Jun Ge^a, Robert Reedy^a, Bridget Scanlon^a

^a Bureau of Economic Geology, Jackson School of Geosciences, The University of Texas at Austin, P.O. Box X, Austin, TX 78713-8924, United States of America

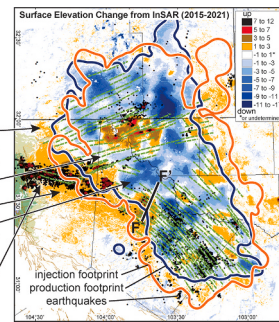
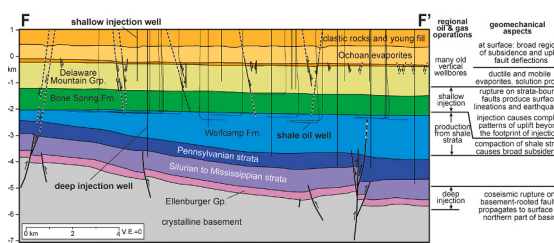
^b Department of Aerospace Engineering and Engineering Mechanics, The University of Texas at Austin, Austin, TX 78713-8924, United States of America

HIGHLIGHTS

- InSAR data reveal complex and accelerating uplift and subsidence in Delaware Basin.
- The magnitude of subsidence is linearly related to oil production.
- The patterns of uplift are complex and caused by pressurization of shallow strata.
- The pattern of faulting is densifying, accelerating and includes coseismic deformation.
- Multiple lines of evidence suggest directional pore pressure diffusion and uplift.

GRAPHICAL ABSTRACT

Between 2015 and 2021 the Delaware Basin as a whole developed significant and complex patterns of anthropogenic surface deformation caused by production of oil and water from shale reservoirs, injection into shallow strata, coseismic rupture, and development of lineations at the ground surface



ARTICLE INFO

Editor: Daniel Alessi

Keywords:
InSAR
Uplift
Subsidence
Coseismic deformation
Neotectonic faulting
Induced seismicity

ABSTRACT

The Delaware Basin in west Texas and southeast New Mexico is now the largest global oil producing basin, averaging $\sim 400,000 \text{ m}^3$ ($\sim 2,500,000$ barrels) per day in 2022. The shale-dominated strata targeted for production can co-produce 4–5 times more water than oil, necessitating disposal by injection of $\sim 1,400,000 \text{ m}^3$ ($\sim 8,700,000$ barrels) of water per day in 2022. Through a comprehensive assimilation of regional Sentinel-1 satellite radar data and analysis of production and injection, we show how petroleum operations have caused the development of complex and accelerating patterns of surface deformation from 2015 through 2021. We observe uplift from reservoir swelling, subsidence from reservoir contraction, and the development of linear features that are indicative of faulting. Subsidence is predominantly caused by production, and an important finding of this study is that the magnitude of subsidence is linearly proportional to total production. Uplift is caused by pressurization from wastewater injection of shallow permeable strata. The patterns of uplift are complex and extend laterally well-beyond areas where injection was performed. Linear surface deformation features are observed throughout the Delaware Basin, and they are lengthening and densifying as uplift and subsidence accelerate. Many of the lineations can be linked to known strata-bounded faults and shallow seismicity in the southern Delaware Basin where they serve as permeable and anisotropic conduits for pore pressure migration. In the Northern Delaware Basin, co-seismic rupture is hosted along basement-rooted faults that may link to the linear surface features. Understanding these dynamic changes in Delaware Basin is a pressing concern for management of subsurface reservoirs and safeguarding the surface environment. Concerns include ongoing

* Corresponding author.

E-mail address: peter.hennings@beg.utexas.edu (P. Hennings).



induced seismicity, hazard of drilling through over-pressured strata, maintenance of integrity for newer wellbores, mitigation of flows of brine and petroleum fluids at the surface of old wellbores, and management of the pore space resource for wastewater injection.

1. Introduction

The Delaware Basin is a sub-region of the Permian Basin province of West Texas and Southeast New Mexico (Ewing, 2019), which is defined structurally by a complex network of basement-rooted faults that formed in Mississippian through Permian time in the foreland of the Ouachita-Marathon Orogeny (Horne et al., 2021) (Fig. 1a). The region has been subject to additional tectonic influences since its formation including renewed contraction during the Laramide Orogeny, extension during Basin and Range tectonism, and uplift and tilting commensurate with its position on the east flank of the Rio Grande Rift. These influences have caused exhumation and erosion, especially along the western flank of the basin, and the creation of thousands of faults, principally of normal offset, that crop out on the flanks of the basin to the west and south (GAT, 2014).

While petroleum has been produced in the Delaware Basin since the 1920s, the implementation of horizontal drilling and hydraulic fracturing starting in ~2009 enabled dramatic acceleration of production. By mid-2022, the Delaware Basin of west Texas and southeast New Mexico had become the world's most prolific oil producing basin, with ~4 billion barrels produced from ~14,000 unconventional horizontal wells between 2010 and 2021 (Fig. 2). As compared to other regions with production of petroleum from shale, the Delaware Basin is exceptionally wet, and the fraction of co-produced formation water typically exceeds that of oil by a factor of 3–4× (Scanlon et al., 2020). Limitations in water treatment techniques and associated economic considerations result in most of this co-produced oilfield wastewater being injected into geologically confined formations (TPWC, 2022; Reedy and Scanlon, 2022). The yearly volumes of wastewater injection track volumes of oil and co-produced formation water. By the end of 2021, 415 million m³ of wastewater were injected into the basin for disposal per month (Fig. 2), and it is estimated that as much as 40 billion m³ of wastewater injection may occur in the basin associated with future production of 12 billion m³ of oil over the ~50-year life of the oil field (Scanlon et al., 2020).

Injection of oilfield wastewater has occurred into strata both below and above the oil-producing shale formations (known as deep and shallow injection, respectively; Figs. 1b and 2). Deep injection principally targets carbonate-rich Silurian and Devonian age strata in the northern portion of the basin, mainly in New Mexico, and in the northeastern corner of Culberson County and northern Reeves County in Texas, totaling 366 million m³ from 2010 through 2021. Significant anomalous seismicity (Hennings et al., 2021; TexNet, 2021, 2022; NMTSO, 2021; Frohlich et al., 2020), hosted along faults rooted in the geologic basement in this region, has been quantitatively associated to pore pressure increase associated with deep injection (Skoumal et al., 2020; Savvaidis et al., 2020; Zhai et al., 2021; Grigoratos et al., 2022). Shallow injection wells target sandstone strata in the Permian-age Delaware Mountain Group (DMG) (Smee et al., 2021; Ge et al., 2022). In New Mexico, injection into the DMG has been minimal since ~2016 due to concerns about negative impacts on existing oil production (Lemons et al., 2019). In Texas, 1.8 billion m³ of wastewater have been injected into these shallow strata from 2010 through 2021. The monthly volume of this injection has increased significantly in recent years, although it declined somewhat during the COVID pandemic due to depression of oil and gas commodity price (Fig. 2). Zhai et al. (2021) use poroelastic models of shallow injection to postulate that stress change may be able to propagate sufficiently downward to destabilize basement-rooted faults to produce seismic rupture. Although fluid injection for hydraulic fracturing has been shown to contribute to seismicity to a minor degree (Skoumal et al., 2020; Savvaidis et al., 2020;

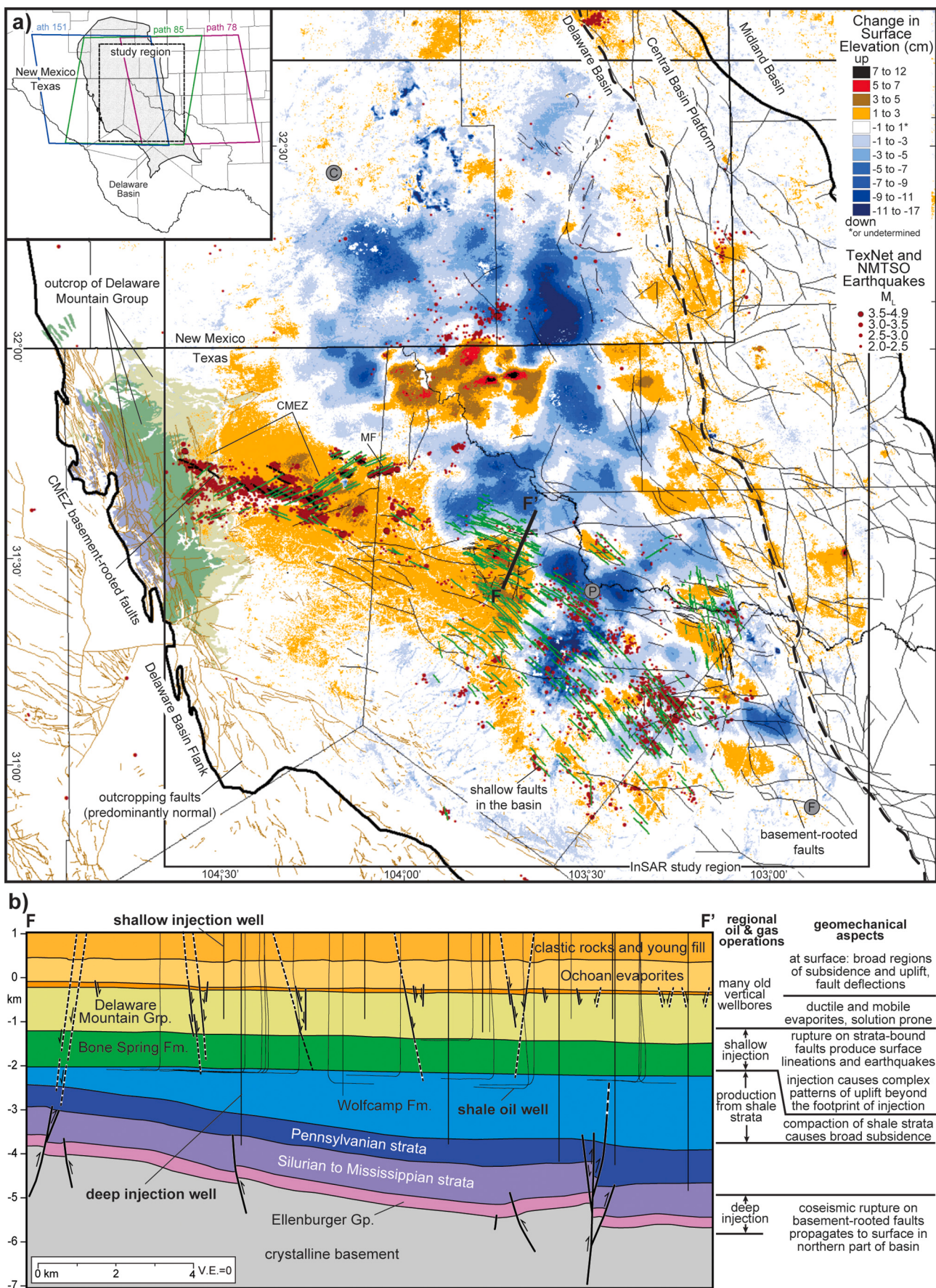
Grigoratos et al., 2022), shallow injection for permanent disposal has been associated quantitatively with rupture and earthquakes on (shallow) strata-bound faults that transect the upper parts of the productive shale formations up through the Delaware Mountain Group (Hennings et al., 2021; Savvaidis et al., 2020; Grigoratos et al., 2022; Horne et al., 2022; Staniewicz et al., 2020; Pepin et al., 2022; Sheng et al., 2022). Rock above the DMG is dominated by 150–1500 m of strata rich in evaporites which are considered to be effective seals and vertically confine fluid and pressure changes from the injection below (Smee et al., 2021). The neotectonically-active faults below the evaporites are propagating either discrete displacement and/or folding to the ground surface through these evaporites and the overlying poorly indurated surficial strata.

The injection and production reservoirs in the Delaware Basin are remarkably dynamic. Through a comprehensive integration of injection data, production data, high-resolution seismic catalogs, and recently mapped fault lines, we document the oil production and wastewater injection activities that caused widespread and complex surface deformation patterns for the entire producing region of the Delaware Basin as observable by Sentinel-1 Interferometric Synthetic Aperture Radar (InSAR) satellites. We interpret these observed uplift and subsidence patterns as reflecting significant geomechanical sensitivity of the subsurface including compaction of petroleum reservoirs; inflation, pressurization, faulting of injection reservoirs with displacements that deflect the ground surface; and induced earthquakes of multiple causes. We show that the distribution of shallow faults has increased in number, densified, spread laterally, and act as conduits affecting the directional diffusion of pore pressure. We discuss how our integrated data sets and findings can be applied for hazard assessment and sustainable development of the basin including (1) optimization of models of future oil production and the associated water handling requirements; (2) optimization of models of injection that can be used for management of the injection strata as a shared resource; (3) assessment of pore pressure evolution for overburden containment assurance, protection of groundwater resources, and assessment of the hazard that pressurization and vertical strain may pose to the thousands of vertical petroleum wells that date back to the 1920s; (4) induced seismicity hazard assessment; and (5) application to reservoir characterization and reservoir dynamics research.

2. Methods and data

2.1. Experimental design

We quantitatively compare spatial and temporal changes in vertical deformation patterns throughout the Delaware Basin using InSAR data acquired between January 2015 and 2021 with numerous measures of subsurface perturbation from fluid withdrawal and injection. We choose the use of annual periods for simplicity in description. We also make comparisons to interpretations of active faults and well-recorded earthquakes. We consider periods corresponding to the availability of both high-quality InSAR data and controls on subsurface perturbation: Jan 1, 2015 to Dec 31, 2018 (the initial 4 years) and Jan 1, 2015 to Dec 31, 2021 (the entire 7 years). It is our approach to focus on longer time periods of summed InSAR deformation for our analysis and integration. Additionally, we solve for 2-year InSAR cumulative vertical deformation for the equal periods of 2016–2017, 2018–2019, and 2020–2021 to capture the spatiotemporal evolution of surface deformation.



(caption on next page)

Fig. 1. a. Map of InSAR-observed cumulative vertical deformation between 2015 and 2021 over the Delaware Basin. Basement-rooted (Horne et al., 2021) and shallow faults (Horne et al., 2022) in the basin subsurface are shown as black and green lines respectively. Outcropping faults (Geologic Atlas of Texas, 2014) are shown as dark yellow lines. Earthquakes that occurred between 2017 and 2021 (TexNet, 2021; NMTSO, 2021) are shown as red dots. Inset map shows the location of the study site and the InSAR flight path used. Grey circles: C = Carlsbad, NM; P = Pecos, TX; F = Fort Stockton, TX. b). Cross section of the central Delaware Basin as indicated by trace F-F' in a. Text on the right indicates the depth and type of principal oilfield activity as well as aspects of geomechanical behavior for observed phenomena as described in the main text. (Fig. modified after Hennings et al., 2021).

2.2. InSAR data processing

Using a geocoded SLC processor (Zheng and Zebker, 2017), we process Sentinel-1 data acquired between November 2014 and December 2021: 151 ascending Path-78 scenes, 147 descending Path-85 scenes, and 148 ascending Path-151 scenes (Fig. 1 inset). For each SAR acquisition, we generate multilooked interferograms at 180-m pixel spacing between the nearest 20 SAR images (equal to a maximum temporal baseline of 0.75–1.5 years, depending on the frequency of the acquisitions). No spatial baseline threshold is imposed in the interferogram formation. Here the impact of closure phase bias from short-term interferograms is negligible (Zheng et al., 2022; Maghsoudi et al., 2022), because InSAR solutions derived from interferograms subsets with longer temporal baselines (nearest 30- and nearest 50-acquisition networks) do not show substantial differences from the results presented in this paper. We unwrap all interferograms using the Statistical-cost, Network-flow Algorithm for Phase Unwrapping (SNAPHU; Chen and Zebker, 2001). We remove long-wavelength phase ramps caused by atmospheric noise using a quadratic phase model. We choose the GPS station TXKM as the reference point for ascending Path 78 and descending Path 85 InSAR data, and we use the remaining stations as controls to assess InSAR measurement uncertainty independently. The Path 151 footprint does not contain GPS station TXKM; for this data, we fit and remove a phase-elevation trend from all high-coherence pixels in each interferogram and zero-reference the deformation (Zebker, 2021). The locations of the available GPS stations in each Sentinel-1 path are

listed in Table S4-S6, and the GPS time series can be accessed through an interactive map at the Nevada Geodetic Laboratory (Blewitt et al., 2018).

The phase of an interferogram can be written as the sum of deformation and multiple noise components:

$$\Delta\phi = \frac{4\pi}{\lambda} \Delta d + \Delta\phi_{tropo} + \Delta\phi_{iono} + \Delta\phi_{orb} + \Delta\phi_{DEM} + \Delta\phi_{decor} + \Delta\phi_{unwrap} + \Delta\phi_n$$

where λ is the radar wavelength, and Δd is the surface deformation along the radar line-of-sight (LOS) direction. The noise terms include tropospheric and ionospheric noise, orbital errors, DEM inaccuracies, phase decorrelation, unwrapping errors, and other residual noise terms that associated with thermal and soil moisture effects. For the Sentinel-1 West Texas data set, the dominant noise source is turbulent tropospheric noise that is random at the time scales longer than one day (Emardson et al., 2003; Staniewicz et al., 2020).

Consider the case of N SAR images forming M unwrapped interferograms with small baselines. At a pixel of interest, we can define a matrix representation of the M equation SBAS system as:

$$A \phi \approx \Delta\phi$$

where $\phi = [\phi_2, \dots, \phi_N]$ is the unknown phase vector that contains deformation signal and tropospheric noise at each SAR date with respect to the first SAR date. $\Delta\phi = [\Delta\phi_1, \dots, \Delta\phi_M]$ is the known phase values of the M interferograms. A is the $M \times (N - 1)$ matrix. If the i^{th} interfero-

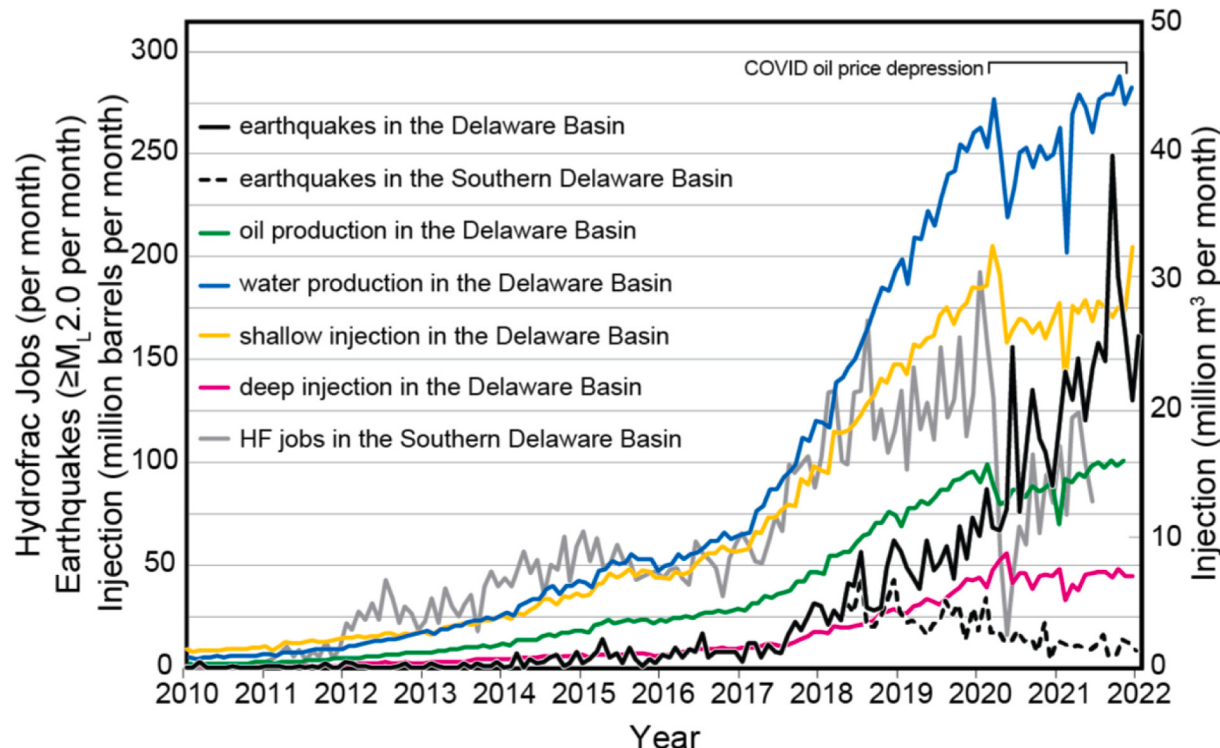


Fig. 2. Trend of production and injection in the Delaware Basin. Monthly production of oil and water, injection of wastewater, and ML ≥ 2.0 earthquakes for the entire Delaware Basin and the southern Delaware Basin between 2010 to 2021. Monthly rate of hydraulic fracturing jobs for the southern Delaware Basin is also shown. Earthquake sources Froehlich et al., 2020; TexNet, 2021; NMTSO, 2021).

gram measures the InSAR phase $\Delta\phi_i$ between data acquisition times t_m and t_n , then the A matrix has -1 in the m^{th} row, 1 in the n^{th} row, and 0 elsewhere. We solve for ϕ using a weighted least squares scheme⁴⁵:

$$\hat{\phi} = (A^T W A)^{-1} A^T W \Delta\phi$$

where $\hat{\phi} = [\hat{\phi}_1, \dots, \hat{\phi}_N]$ is the estimated phase time series, and W is the $M \times M$ diagonal weight matrix. We employ the weighting scheme $W_{ii} = 1/T_i$, where T_i is the temporal baseline of the i^{th} interferogram.

Based on the inversion results, we mask out all pixels which have a temporal coherence lower than 0.75 (Yunjun et al., 2019) or an average spatial coherence of <0.2 . To remove turbulent tropospheric noise, we perform a temporal smoothing of the InSAR time series solution $\hat{\phi} = [\hat{\phi}_1, \dots, \hat{\phi}_N]$ using the robust Locally Weighted Scatterplot Smoothing (LOWESS) technique (Ferretti et al., 2001). The LOWESS smoothing algorithm is a temporal filtering step similar to the triangular filtering step (Cleveland, 1979; Berardino et al., 2002). The advantage of using the adaptive LOWESS filter instead of a fixed-window filter is that SAR acquisitions that contain severe tropospheric noise artifacts (e.g., due to heat waves or heavy storms) are down-weighted or ignored in the final surface deformation estimates.

To assess the performance of the LOWESS-smoothed LOS deformation results, we project the available GPS ENU time series onto the radar LOS using the local line-of-sight vectors. For Paths 78, 85, and 151, there are 15, 10, and 3 GPS stations available for comparison (respectively). We smooth each GPS time series x with a 180-day moving window, and compare GPS and InSAR observations at each of the N SAR acquisitions. We calculated the root-mean-squared (RMS) difference between InSAR and GPS as

$$\text{error}_{\text{RMS}} = \sqrt{\frac{1}{N} \sum_{j=1}^N (x_j - \hat{\phi}_{j,\text{LOWESS}})^2}$$

where x_j indicates the GPS point at the same time as the j^{th} SAR acquisition. We also compute the maximum absolute difference between the InSAR solutions and the GPS time series, $\max_{j=1,\dots,N} |x_j - \hat{\phi}_j|$. For Path 78, there is an average of 3 mm RMS difference between the smoothed GPS time series and the InSAR LOWESS solutions across all time steps (Table S1). The maximum absolute difference at any time between GPS and InSAR is 1.3 cm. For descending Path 85, the average RMS difference is 5 mm, and the maximum absolute difference is 1.4 cm (Table S2). For ascending Path 151, the average RMS difference is 3 mm, and the maximum absolute difference is 8.5 mm (Table S3). After assessing the InSAR errors along the LOS direction, we decompose overlapping ascending and descending acquisitions into vertical and horizontal deformations as described in Staniewicz et al., 2020.

In our analysis we use the vertical component of the processed InSAR data as it has been shown by others (e.g., Pepin et al., 2022) that the horizontal component of the surface deformation in the Delaware basin is minor as compared to the vertical component. Sentinel-1 imaging geometries are not sensitive to northward motion, and uncertainty in estimates of eastward deformation are considerably larger than estimates of vertical deformation.

2.3. Earthquakes

We compile well-recorded earthquakes in the Delaware Basin from 2017 to 21 (Figs. 1a, 2, 4d, 5d) from TexNet (2021), relocated earthquakes TexNet (2022), and from the NMTSO (2021). Generalized locations of earthquakes in the Delaware Basin region from 2010 to 2018 are also available (Frohlich et al., 2020).

2.4. Production data

We compile well design and fluid production data from wells in the Delaware Basin from public sources including the Railroad Commission of Texas (RRC) and the New Mexico Oil Conservation Division (NMOCD) using the S&P Enerdeq analytical tool (see Data Availability). Fluid production data is compiled on a per well basis from 12,767 horizontal wells completed in the Bone Spring and Wolfcamp Formations that produced within the 2015–21 temporal window. To capture volumes from vertically stacked wells, produced oil and water volumes are summed for each 2.59 km^2 (1 mi^2) block for the 2015–18 and 2015–21 temporal windows. Produced volumes per unit area are interpolated from center points using kriging with a 100 point search radius and spherical semivariogram to represent the smoothed density of fluid withdrawal while maintaining the overall magnitude of fluid volumes withdrawn across the basin. Produced gas volumes are not included in the analysis because gas likely does not exist in appreciable quantities in Bone Spring and Wolfcamp Formations at reservoir depth, but rather is emitted from the liquid phase at reduced pressures during production.

2.5. Injection data and pore pressure

We compile information on injection wells in the Delaware Basin from public sources including the RRC and the NMOCD using the private vendor S&P Enerdeq and B3 Insight analytical tools. We use records of well design to determine the depth and stratigraphic level of injection for each well and we gather monthly injection volumes for summation as per the two chosen temporal windows. For pore pressure evolution in the DMG we use published data (Ge et al., 2022) for the end-2018 temporal window. For the end-2021 temporal window we use the most recent injection data to determine the pore pressure evolution in the DMG by directly extending our existing published reservoir characterization (Smee et al., 2021) and the calibrated hydrogeologic model (Ge et al., 2022).

2.6. InSAR fault lineation analysis

To assess how subsurface faulting may be reflected in the development of linear patterns in our InSAR deformation maps we trace all surficial lineations from our two temporal windows. In contrast to the recent mapping of basement-rooted faults (Horne et al., 2021) and shallow rootless faults (Horne et al., 2022) in the Delaware Basin where subsurface data was employed in the interpretation (Fig. 1a), we rely only on InSAR lineations that develop within our two temporal windows. We map linear features that are at least 5 km in trace length. We consider these lineations to be indicative of neotectonically active subsurface faulting, especially as they coincide in both location and strike with many faults mapped using subsurface data. They also agree very closely with the trend of maximum horizontal stress (S_{Hmax}) (Dvory and Zoback, 2021a).

3. Results

3.1. InSAR surface deformation observations

We observe maximum uplift (positive values) and subsidence (negative values) of 6 and -9 cm for 2016–17, 6 and -11 cm for 2018–19, and 8 and -16 cm for 2020–21 (Figs. 3a–c). During the period of 2016–17, distinct areas of local subsidence and uplift are evident. For 2018–19 and 2020–21, most of those local areas persisted. In two notable cases, uplift area U6 and subsidence area S4 each occupied substantially larger footprints with each sequential time increment.

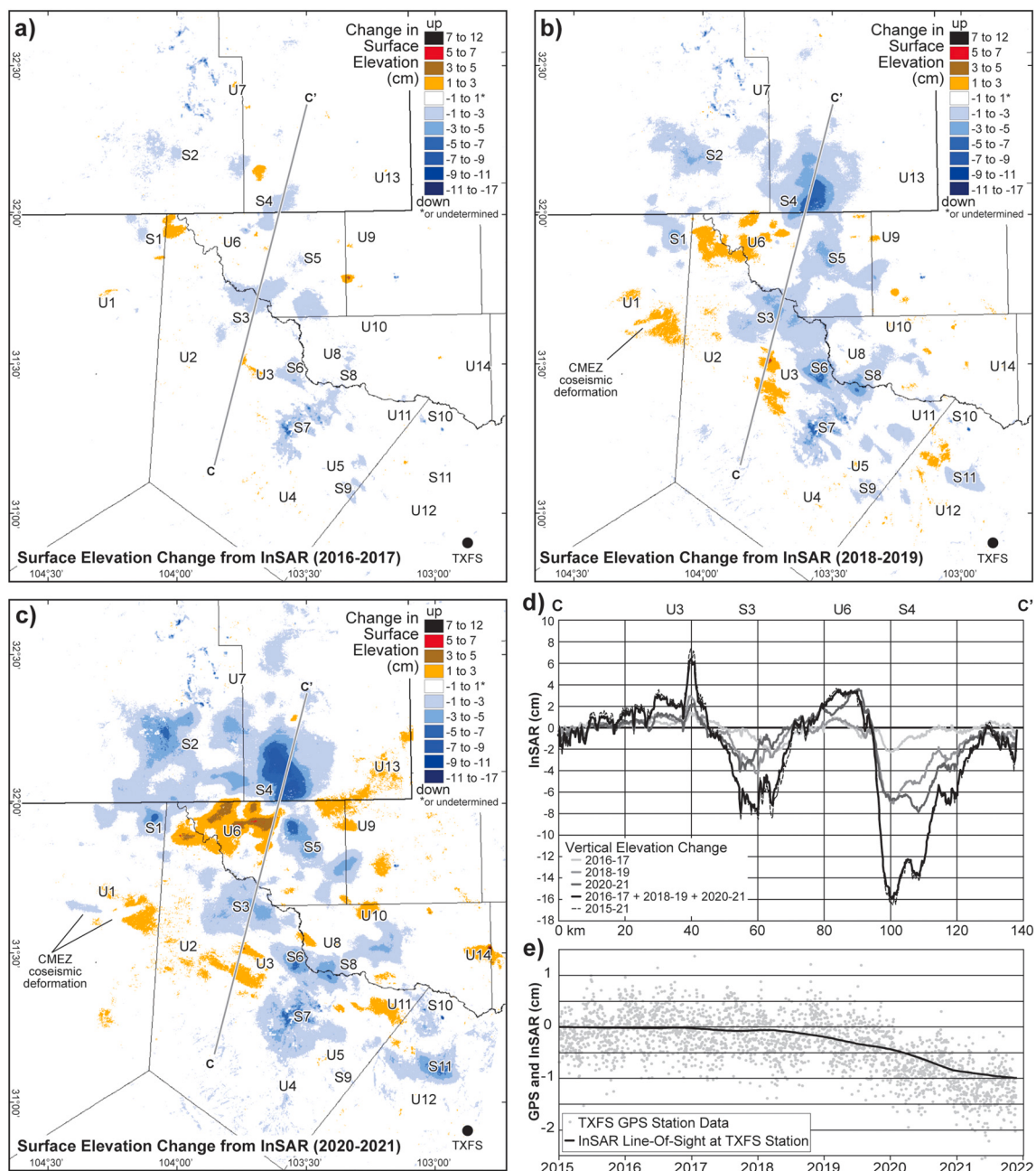


Fig. 3. a-c). Maps of InSAR-observed cumulative vertical deformation over the Delaware Basin for 2016-17, 2018-19, and 2020-21, respectively. Labels indicate individual areas of uplift and subsidence as discussed in the text. d). Time series of elevation change along profile C-C' for the InSAR maps in 3a-c, the sum of those 3 maps, and the total for 2015-202 as per Fig. 5a. e). Time series data for the GPS station TXFS and sampling our InSAR Line-Of-Sight data at the TXFS location. See a-c for location of TXFS.

Subsidence area S3 was most localized in 2016–17, and then broadened but became less pronounced in 2018–19 and 2020–21. Fig. 3d shows the vertical deformation as sampled along the profile C-C', which demonstrates the relative rates and degree of lateral shift of vertical deformation over time. The profile also shows the sum of the three time periods, as well as the entire 2015–21 InSAR record studied as shown in Figs. 1a and 5a.

Comparison of the sum of 2016–17, 2018–9, and 2020–21 vs 2015–21 shows how uplift and subsidence was minimal along the sampling profile in the year of 2015. The InSAR deformation and GPS station elevation change and GPS station TXFS is shown in Fig. 3d. Note that there is some seasonal signal in the GPS data which our InSAR smoothing approach nicely removes.

During the entire 7 years of study period (2015–2021), we observe up to 17 cm subsidence over a region extending ~215 km from Carlsbad, NM to Fort Stockton, TX with a width ranging from ~30 to ~90 km (Fig. 5a). The existence of the subsided area was apparent by the end of 2018 where the subsidence occurred in more isolated and discontinuous depressions (regions) (Fig. 4a). The subsided regions coalesced into a pronounced and broad elliptical area by 2021, but still containing isolated pockets of greater subsidence (Fig. 5a). The total area experiencing subsidence through 2021 was ~16,600 km² and the rock volume that subsided increased from 130 Mm³ through 2018 to 330 Mm³ through 2021 (130 Mm³ in 4 years followed by 200 Mm³ in 3 years) (M = million). The most significant subsided regions are labeled as S1-S11 in Figs. 3, 4a and 5a.

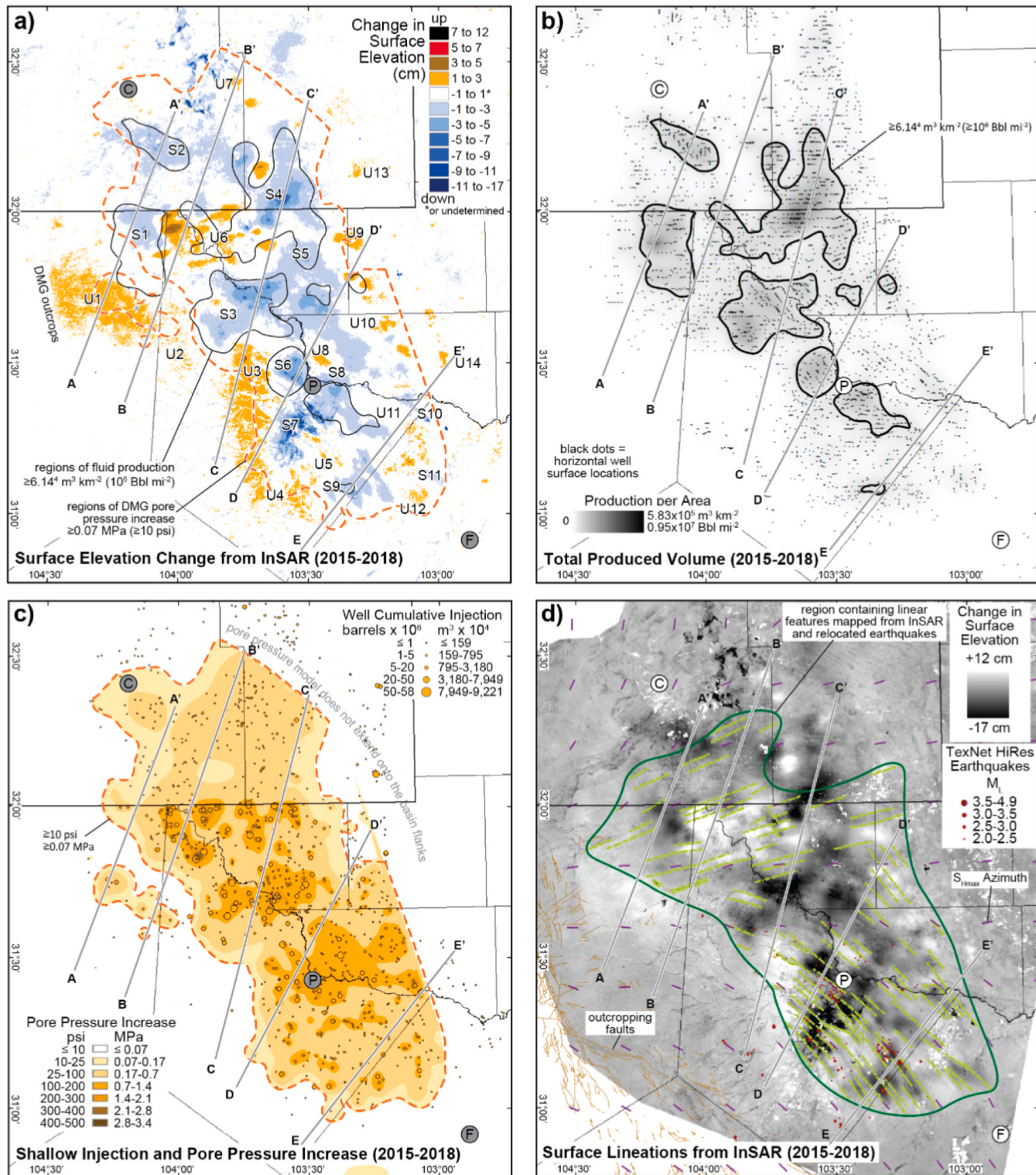


Fig. 4. Maps for the 2015-2018 period (4 years). a) InSAR-observed cumulative vertical surface displacement. Regions of minimum fluid production are taken from Fig. 4b, and regions of minimum pore pressure increase are taken from Fig. 4c. Regions marked with S1-S10 are specific subsidence regions, and regions marked with U1-U14 are specific uplift regions. Deformation profiles A-E are shown in Fig. 6. b) Total fluid production from shale strata. c) ΔP_p in the DMG from shallow injection (modified after Ge et al., 2022) and the cumulative volume injection at each injection well. d) Distribution of linear features as observed from the InSAR surface deformation map and relocated earthquakes. Some of these features are coincident with mapped faults (Horne et al., 2022), and some are interpreted as possible zones of faulting in the subsurface. The azimuth of S_{Hmax} is indicated (Dvory and Zoback, 2021a, b). The region of linear features is enclosed by the dark green line.

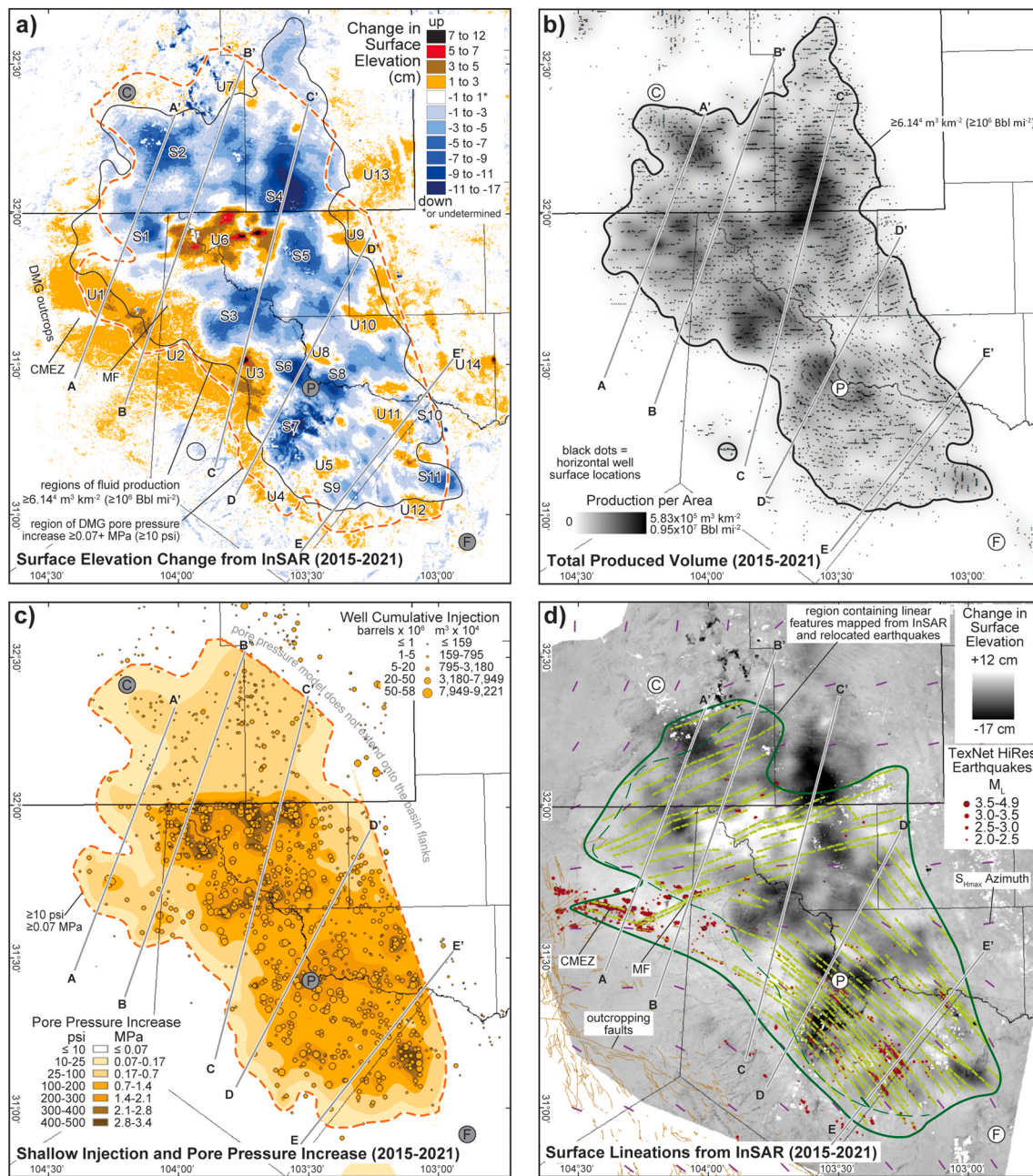


Fig. 5. Maps for the 2015–2021 period (7 years). a). InSAR-observed cumulative vertical surface displacement. Regions of minimum fluid production are taken from Fig. 4b, and regions of minimum pore pressure increase are taken from Fig. 4c. Regions marked with S1–S10 are specific subsidence regions, and regions marked with U1–U14 are specific uplift regions. Deformation profiles A–E are shown in Fig. 6. b). Total fluid production from shale strata. c). ΔP_p in the DMG from shallow injection (modified after Ge et al., 2022) and the cumulative volume injection at each injection well. d). Distribution of linear features as observed from the InSAR surface deformation map and relocated earthquakes. Some of these features are coincident with mapped faults (Horne et al., 2022), and some are interpreted as possible zones of faulting in the subsurface. The azimuth of SHmax is indicated (Dvory and Zoback, 2021a, b). The region of linear features is enclosed by the dark green line.

We observe up to 12 cm of uplift between 2015 and 2021 in regions generally peripheral to, or surrounded by subsidence features (Fig. 5a). The most significant uplift regions are labeled as U1–U14 in Figs. 3, 4a and 5a. These areas of uplift were established by 2018, and each became accentuated by 2021. Region U6 became especially prominent by 2021, in essence rising out of an area otherwise dominated by subsidence (Fig. 5a). In addition, a large region of uplift spanning U1 to U3 developed along the western margin of the basin (Figs. 1a, 5a). The boundary of the uplift feature coincides closely with the shape of the erosional pattern of the outcrop of the DMG. The total area experiencing uplift for 2015–21 was ~18,200 km². The rock volume that uplifted increased

from 84 Mm³ through 2018 to 155 M³ through 2021 (84 Mm³ in 4 years followed by 71 Mm³ in 3 years). In Fig. 6 we show a series of data profiles that sample elevation change, production, injection, pore pressure change, and the locations of surface lineations for 2015–18 and 2015–21 as described in the sections that follow.

3.2. Petroleum fluid production trends

Maps of oil and water produced from shale strata for each temporal window are shown in Figs. 4b and 5b, along with the location of the producing wells. Through 2018, a large area of production was

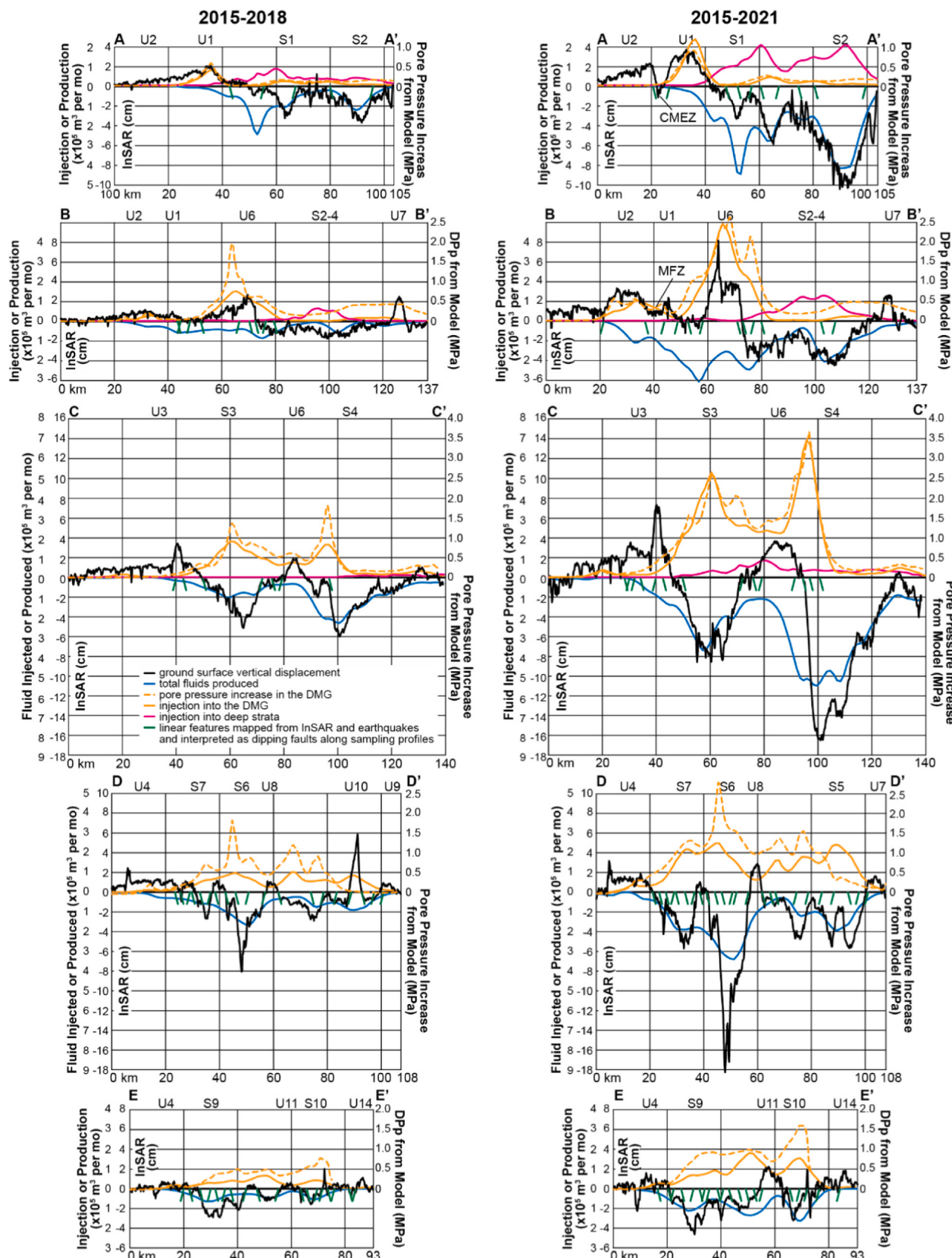


Fig. 6. Vertical deformation and agents of causation along 5 profiles. The panels on left are results of the 2015-18 period, and the panels on right are results of the 2015-21 period. The profile traces are shown in Figs. 4 and 5.

established following the trend of the basin, with a maximum volume produced of $\sim 250,000 \text{ m}^3/\text{km}^2$ based on smoothed produced volume data, and a mean of $\sim 6100 \text{ m}^3/\text{km}^2$. Through 2021, the production footprint remained static, but the maximum volume produced increased to $\sim 600,000 \text{ m}^3/\text{km}^2$ with a mean of $\sim 18,500 \text{ m}^3/\text{km}^2$. For spatial comparison, the isolines of injection in Figs. 4b and 5b are shown in Figs. 4a and 5a, respectively.

3.3. Wastewater injection trends

Maps of injection wells, cumulative volume injected, and contours of volume injected are shown in Fig. S1. Figs. S1a and b show the trends for injection into the DMG and demonstrate the contrast where this injection has been widely permitted in the Texas portion of the Delaware Basin but has been minimal in New Mexico in recent years. Note the significant volumes injected immediately south of the TX/NM border as well as other areas farther south in the basin. Figs. S1c and d show the trends for injection into deep strata below the shale oil reservoirs and above basement. Most of this injection has occurred in New Mexico but ~ 20 deep injection wells operated in Texas during our study period.

3.4. Pore pressure increase trends

Maps of the predicted pore pressure increase (ΔP_p) in the DMG modeled through 2018 and 2021 are shown in Figs. 4c and 5c, respectively. Cumulative volume injected per well is also indicated. A broad region of ΔP_p exceeding 0.07 MPa extended throughout the basin by the end of 2018. Several areas experienced $\Delta P_p \geq 2 \text{ MPa}$ in Texas. By the end of 2021, regions experiencing $\Delta P_p \geq 2 \text{ MPa}$ had become widespread throughout the Texas portion of the basin.

3.5. Development of linear features at the ground surface and relationship to earthquakes

Expanding on the published interpretation of shallow faults in the Delaware Basin (Hennings et al., 2021; Horne et al., 2022), we observe a broad region with linear features observable at the ground surface throughout the basin. As observed in the 2015–2018 cumulative surface deformation map (Fig. 4d), the impacted area covered $\sim 11,700 \text{ km}^2$ and the total trace length of the lineations was $\sim 1500 \text{ km}$. The 2015–2021 cumulative surface deformation map (Fig. 5d) shows an increase in the number of linear features, lengthening and/or joining of existing features, an increase in the impacted area to $\sim 13,800 \text{ km}^2$, and a total trace length of $\sim 2800 \text{ km}$. This represents a lineation densification of $\sim 87\%$ for 2018–2021 within a footprint that increased by $\sim 18\%$. In the southern parts of the basin, the linear features closely follow previously mapped shallow faults (Figs. 1a and b) and relocated earthquakes (Figs. 4d and 5d). The lineations closely parallel the azimuth of S_{Hmax} (Figs. 4d and 5d, Dvory and Zoback, 2021a). We conclude that these linear features are subtle, yet organized flexures expressed at the ground surface that are indicative of faulting in the subsurface. Many coincide with sharp boundaries of subsided and uplifted regions such as the boundary between S4 and U6 along the TX/MN border.

We show all catalogued earthquakes for 2017–21 on Fig. 1a and relocated earthquakes in Texas for 2017–18 and 2017–21 on Figs. 4d and 5d, respectively. While linear clusters of earthquakes occurring along the shallow faults in the Delaware Basin subsurface is well-established (Hennings et al., 2021; Horne et al., 2022), deciphering the associated co-seismic deformation is difficult in most areas of the basin due to the impact of subsidence from production and uplift from injection. However, there is a prominent case where earthquake activity has produced a newly-developed pattern of surface deformation in an area devoid of local production and injection. A graben-like feature developed during the 2019–21 period called the Culberson-Mentone Earthquake Zone (CMEZ) (Figs. 1a, 5a). Beginning in mid-2018 and continuing through 2021, >3100 earthquakes of $M_L \geq 2.0$ with

magnitudes up to ML4.9 occurred in CMEZ. This seismicity and associated faulting have created a graben-like structure in the InSAR data $\sim 20 \text{ km}$ long and $\sim 5 \text{ km}$ wide and elevation relief of up to 6 cm across the structure (Fig. 6, 2015–2021 profile A-A'). A second case is the Mentone Fault Zone that ruptured with a magnitude $M_L 4.9$ in 2020 and has had over 80 earthquakes of $M_L \geq 2.0$. This cluster of earthquakes is associated with a narrow trough-like feature $\sim 10 \text{ km}$ long and $\sim 2\text{--}3 \text{ km}$ wide and 2–3 cm of elevation relief across the zone (Figs. 1a, 5a; Fig. 6, 2015–21 profile B-B').

3.6. Relationship between fluid production and subsidence

Except for the areas where uplift from injection dominates, there is a strong spatial correspondence between the footprint of fluid production from Permian shale (Fig. 1b) and subsidence in both the 2015–18 and 2015–21 study periods (see regions of fluid production to patterns of subsidence in Figs. 4a, b and 5a, b). Fig. 6 shows visually shows how total produced fluid and observed subsidence are highly correlated (e.g., 2015–21 A-A' S1 and S2; B-B' S2–4; C-C' S3 and S4; D-D' S5, S6, and S7). A comparison of the 2015–18 and the 2015–21 results illustrate the acceleration of this coupling in 2019 through 2021 (Fig. 6; e.g., profile C-C').

Importantly, the absence of shallow injection into the DMG in New Mexico allows for quantitative assessment of production-related subsidence in areas free of the negating impact of uplift from shallow injection (Figs. 7a and b). We find a strong linear relationship between production and subsidence in the S2 and S4 subsidence regions in both 2015–18 and 2015–21 periods. The specific regions sampled for this analysis are indicated in Fig. S3. Subsidence at depth becomes mechanically attenuated at shallower levels (Segall, 1992). Therefore, as compared to the ground surface response, the actual change in elevation of strata subsiding due to compaction would be greater for horizons at depth, such as the top of the Wolfcamp Formation (Fig. 1b).

Groundwater production can also produce subsidence therefore we have endeavored to assess those production trends and relate them to subsidence (Galloway et al., 1999). Throughout the Delaware Basin, water is produced from shallow sources for crop irrigation, livestock, municipal and domestic supply, drilling rig supply (drilling mud, etc.), and for hydraulic fracturing. Water use values by category are available in Texas from the Texas Water Development Board annually for 2015 through 2019. Information of water well locations and intended use are available from the Texas Department of Licensing and Regulation Submitted Driller Reports database, which contains reports for all water wells completed in Texas since about 2002. Water use values for New Mexico are available from the USGS but only through 2015 as per the time of this writing. We therefore focus our analysis on Texas (see Supplementary Text for additional information about groundwater wells and water production history).

Water use in the Texas portion of the Delaware Basin is dominated by crop irrigation followed by uses for hydraulic fracturing, municipal supply, and for livestock (Table S4, Fig. S2a). The principal groundwater source covering the majority of the subsided area is the Pecos Valley Aquifer (Texas Ground Water Development Board Groundwater Database, see Data Availability). The overall water usage in the Texas counties of the Delaware Basin was relatively constant, averaging $\sim 3 \times 10^8 \text{ m}^3$ between year 2015 and 2019 (Fig. S2a, Table S4). We also compile recent hydrograph data acquired from 28 wells since 2018 in the same region (Fig. S2b and c, Table S5). At each well, we qualitatively classify the trend of depth to water over the 2015–18 period as either no significant change or deepening. A deepening of the water level in confined aquifers should produce ground surface subsidence. From this analysis, we observe no clear relationship between changes in water level in the wells and InSAR subsidence over the same period. Given that there is (1) little correlation between water levels in groundwater production wells and areas of subsidence; (2) no significant increase in the rate of shallow water production regionally, and (3) a significant

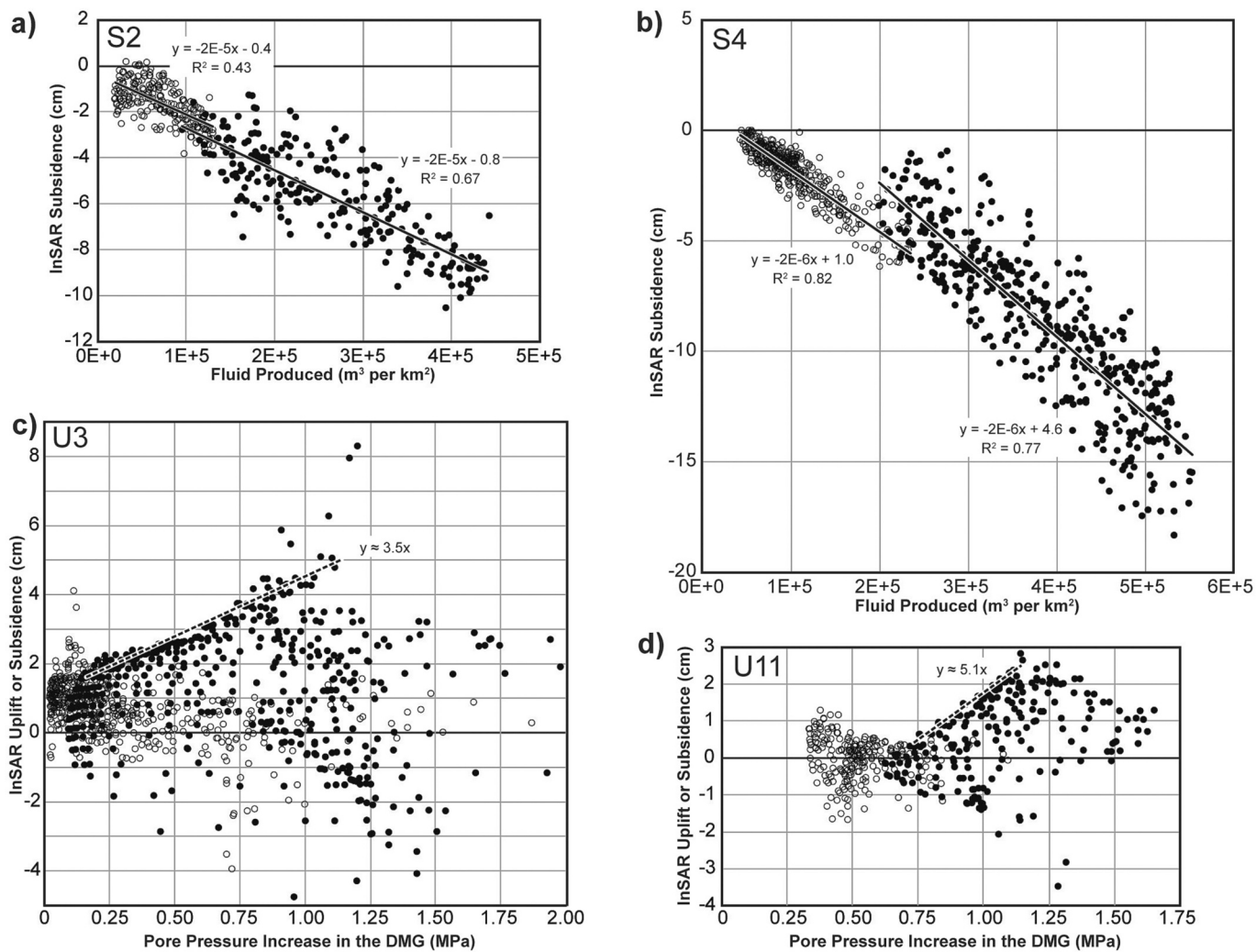


Fig. 7. Relationship between fluid production and subsidence, and injection and uplift. Total fluid production vs. subsidence for the period of 2015–18 (open circles) and 2015–21 (filled circles) for in sub-region S2 (a) and sub-region S4 (b). Estimated ΔP_p in the DMG vs. subsidence for the period of 2015–18 (open circles) and 2015–21 (filled circles) in sub-region U3 (c) and sub-region U11 (d). The regions of the data sampled are indicated in Fig. S3.

increase in the rate of water and oil produced from shale strata, we conclude that subsidence from production of fluids extracted from shale strata is the overwhelmingly dominant cause of the subsidence we observe as compared to shallow groundwater production. We do observe a notable discrepancy in this finding in the area of S7 where there is significant subsidence in 2015–18 and continuing through 2021 and relatively little local fluid production from shale strata. In the region of S7, there is a concentration of irrigated crop land (Reedy and Scanlon, 2022) and it is also the area where two of the wells in our analysis of depth to water show increasing depth. Therefore, we agree with prior work (Deng et al., 2020) that the principal cause of subsidence in the region of S7 is caused by groundwater production.

3.7. Relationship of injection and uplift

It is well established that injection can cause land surface uplift (Teatini et al., 2011). There are no areas in our study where injection into shallow or deep strata occur without production from shale strata locally. Therefore, we find the pattern of uplift from injection to be complex but apparent (see relationship of fluid injection and ΔP_p to patterns of uplift in Figs. 4a, c and 5a, c). We find local areas where uplift from injection exceeds subsidence from production and manifest as uplifting islands (e.g., regions U5, 6, 7, 8, and 11). These uplift features became considerably more pronounced in recent years, and they are

each closely associated with areas of substantial injection volumes and ΔP_p . For example, the uplift of U11 (2 cm) by the end of 2021 occurred with ΔP_p of ~0.7 MPa, and the uplift of U6 (over 7 cm) occurred with ΔP_p of between 2.1 and 2.8 MPa. The thickness of the DMG overburden ranges from 0.75 to 1.25 km for U6 and 1.5–1.6 km for U11.

We also observe a broad and diffuse halo of uplifted areas peripheral to the region where subsidence dominates along the producing axis of the basin. This peripheral domain of uplift extends to where the DMG outcrops on the western margin of the basin (Figs. 1a, 4a, 5a). These uplift features were apparent by the end of 2018, and each became more pronounced by the end of 2021 (e.g., U1, 2, 3, 4, 7, 9, 12, 13, and 14). In these areas, the associated ΔP_p in the DMG was <1.4 MPa everywhere. The thickness of the DMG overburden ranges 0 to 1.2 km in areas in the western part of the basin to 1.5–1.2 km in the eastern part of the basin. There is little to no injection and ΔP_p associated with the areas of uplift to the west of regions U1–3, and we therefore believe that there must be an increase in DMG reservoir pore pressure that stems from directionally-controlled diffusion and ΔP_p from areas of concentrated injection in the east. Our observation that uplift extends to the outcrop of the DMG in the west is consistent with this belief because the DMG must be present in the subsurface to experience inflation and uplift from ΔP_p . In the Discussion we elaborate on five lines of evidence for directionally-controlled diffusion and ΔP_p and we include fault reactivation in the hypothesis. The pattern of uplift at considerable distances

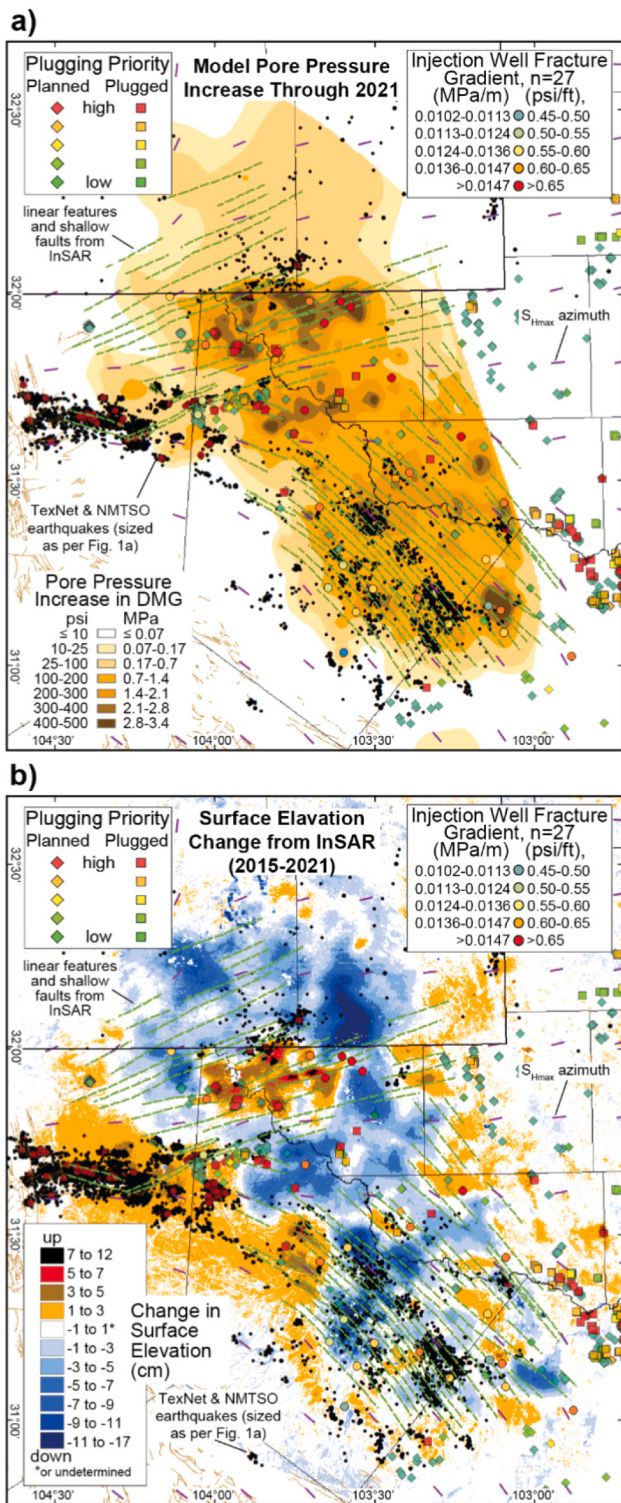


Fig. 8. a) Distribution and priority of wells within the RRC abandoned well plugging program and reported fracture gradient of DMG injection wells from step rate test data on the map of DMG ΔP_p through 2021. b) Same well data as (a) but showing map of InSAR elevation change from 2015-21. The priority criteria for the abandoned wells is described in the text. The interpreted InSAR lineations for 2015-21 from Fig. 5d are shown on both maps.

away from areas of shallow injection being one of the five.

The second line of evidence for directionally-controlled diffusion and ΔP_p from shallow injection comes from distribution of fracture gradient (FG) data as obtained from the RRC for 27 DMG injection wells tested in 2019–21 (Figs. 8a, b; Table S6). This data shows that wells in the areas with shallow faulting and earthquakes in the southern Delaware Basin have lower fracture gradients than wells in the north (≤ 0.0147 vs > 0.0147 MPa/m, respectively; ≤ 0.65 vs > 0.65 psi/ft). We interpret this variation to support our hypothesis of fault activation and directional pore pressure migration because, with injection into the DMG, a lower fracture gradient promotes both the propagation of hydraulic fractures away and upward from the injection well and the reactivation of shallow faults. It is well known that hydraulic fractures open perpendicular to the azimuth of S_{Hmax} and can preferentially conduct fluids along their length (Zhang and Yin, 2017). Faults that rupture with dominantly normal slip everywhere strike (sub)parallel to the azimuth of S_{Hmax} in the southern Delaware Basin. Once brought to the critical stress condition with ΔP_p , with or without rupture, the faults can serve as directional pathways for fluid flow and ΔP_p (Townend and Zoback, 2000; Hennings et al., 2012).

Given that subsidence from production occurs everywhere there is injection into the DMG and ΔP_p , it is not possible to directly quantify uplift from ΔP_p without accounting for subsidence from production. However, there are areas where it can be estimated, especially where rates of production have been locally low. By the end of 2021, region U3 had uplifted by 4–5 cm and the cross plot of ΔP_p vs uplift has a linear upper bound that can be used to estimate that each cm of uplift occurred with a ΔP_p of ~ 0.3 MPa. Similarly, in region U11 each cm of uplift occurred with a ΔP_p of ~ 0.2 MPa.

Using the linear relationships observed for subsidence from production in Fig. 7a and b and uplift from injection, we can distinguish relative roles of injection and production on the complex surface deformation response and provide an independent check on our causal interpretation. The U1 and U2 regions experienced uplift of up to ~ 4 cm by the end of 2021 and very little production, therefore it is our projection, using the average of our U3 and U11 correlations, that the DMG in this area may be experiencing ΔP_p of up to ~ 1.0 MPa, which is generally consistent with our ΔP_p model. By the end of 2021, the U6 region experienced a mean uplift of 2.2 cm, a mean production of $240,000 \text{ m}^3/\text{km}^2$ and a mean ΔP_p of ~ 1.9 MPa. Using the average of the S2 and S4 correlations suggests that the U6 region should have subsided by 5.9 cm. Using the average of the U3 and U11 correlations suggests that the U6 region should have uplifted by 8.4 cm. This leaves us with a predicted uplift of 2.5 cm, quite close to the observed 2.2 cm.

Like subsidence, reservoir inflation at depth becomes mechanically attenuated at shallower levels (Segall, 1992). Compared to the ground surface response, the actual change in elevation of strata uplifted due to ΔP_p would be greater for horizons at depth, such as the top of the DMG (Fig. 1b).

We see no evidence of uplift from deep injection in the northern Delaware Basin where the footprint of deep injection does not coincide with any uplifted regions (Figs. S1c, d compared to Figs. 4a and 5a). If uplift from deep injection were present, we would expect that it would have a broader and lower amplitude wavelength as compared to the footprint of deep injection and it is possible that the uplift is masked by subsidence from production in Culberson County, TX and SE New Mexico.

3.8. Expansion of the vertical section

It is outside our scope here to quantitatively assess co-located expansion of the vertical section caused by subsidence at depth from production and uplift from shallow injection. What we can say, using the linear relationships in Fig. 7, is that there is a maximum of up to 25 cm of vertical expansion predicted for the U6 region (predicted uplift minus predicted subsidence). Given that mechanical attenuation affects our

estimations of both uplift and subsidence, the true vertical expansion in the subsurface (e.g., what the vertical portion of wells experience) would be greater. In locations where there are sharp lateral contrasts between regions of uplift and subsidence, the lateral difference in vertical expansion may give rise to faulting as expressed as linear features on the ground surface (e.g. the boundary between S4 and U6).

3.9. Orphaned wells and plugging priority

It is estimated that there are >100,000 idled petroleum wells in Texas (EDF, see Data Availability). The RRC maintains a database of wells in Texas that are no longer claimed by operators (*orphans*) and is actively plugging these wells according to a ranking scheme or priority (see Data Availability). Priority 1 wells have evidence of active fluid or gas leakage at the surface. In Figs. 8a and b we show the location and priority of 280 *orphaned* wells in the Delaware Basin on maps of DMG ΔP_p and 2015–21 elevation change. We note that the 40 Priority 1 wells occur in areas of the Delaware Basin in Texas where our model predicts an association with a mean DMG ΔP_p of 1.6 MPa as of the end of 2021 for wells currently awaiting plugging. For wells previously plugged, the mean DMG ΔP_p in the nearest year to plugging was 1.2 MPa (Fig. 8a). The location of high priority wells is also biased to areas with uplift (e.g., the mean elevation change of priority 1 wells is +2.1 cm). For this aspect, it is important to note that a tiny percentage of old wells in the Delaware Basin are in the RRC's orphaned well plugging program. Leakage at the surface of *operated* wells is generally not reported publicly and there are approximately 27,000 *operated* wells in the basin that were drilled prior to the onset of horizontal drilling in 2009.

4. Discussion and conclusions

Ongoing development of the Delaware Basin as one of Earth's most prolific hydrocarbon-producing regions should be undertaken with full cognition of surface and subsurface changes associated with development, and the hazards that may be created. The Delaware Basin has shown itself to be geomechanically sensitive with subsidence from compaction of shale due to petroleum production, uplift from reservoir inflation from injection, and pore pressure-driven stress change to reservoirs causing fault rupture and formation of linear elevation changes at the surface. We observe that the rate of both subsidence and uplift has increased rapidly in recent years. In the northern part of the basin, induced earthquakes with $M_L \leq 5.4$ occur associated with deep injection. In the southern Delaware Basin, shallow injection has caused rupture of a well-organized system of existing faults including seismogenic slip with $M_L \leq 3.5$, aseismogenic slip, and many linear deformations of the ground surface. An understanding of the impact can come from analysis of changes to the ground surface, as well as earthquakes induced from petroleum operations, if these data are thoroughly integrated with comprehensive assessments of the causal influences as we present here. Our InSAR surface deformation estimates are validated using independently processed GPS time series acquired at all available permanent stations throughout the basin. More importantly, the observed deformation patterns are directly attributable, spatially and temporally, to the causal influences of production, injection, and faulting.

4.1. Development of linear patterns on the ground surface and relationship to seismicity

Fig. 1a shows faults as recently mapped in the Delaware Basin at the level of the basement-sediment interface (Horne et al., 2021) and shallower, strata-bound faults (Horne et al., 2022). The basement-rooted faults which have been seismogenic are mainly located in the northern Delaware Basin in CMEZ, the Mentone Fault Zone, and in New Mexico (Hennings et al., 2021). This basement-hosted seismicity has been linked to deep injection above basement (Skoumal et al., 2020; Savvaidis et al.,

2020; Zhai et al., 2021; Grigoratos et al., 2022), and rupture on these basement-rooted faults has not been associated with hydraulic fracturing operations (Grigoratos et al., 2022). In CMEZ alone, there were ~4000 $M_L \geq 2.0$ earthquakes that occurred below the basement-sediment interface by mid-2022. We employ the same fault mapping methods as in Horne et al., 2021 and add 22 short basement-rooted faults to the interpretation of CMEZ (Fig. 1a). Fault plane solutions indicate that earthquakes in CMEZ are dominantly dip slip on steeply-dipping faults (Huang et al., 2022). The observed surface deformation in the CMEZ area and along the Mentone Fault Zone is indicative of seismogenic offsets in the basement that have propagated to the ground surface. This behavior is facilitated in CMEZ where basement is much shallower on the western flank of the basin (~1 km MSL) as compared to depths of up to ~4.5 km along the structural axis of the basin. However, there are also shallow faults in the CMEZ area therefore it is possible that some faults in this complex zone may extend upward from the basement vertically to shallow levels, either geologically, or as faults have propagated neotectonically (Figs. 1a and b, 4d, 5d). Modeling of the distribution of cumulative slip as estimated from earthquake moment along with thorough characterization of the stiffness of the various overburden layers could be conducted in the future to ascertain how the patterns of rupture are propagating to the ground surface in this area.

In the southern portion of the Delaware Basin, extensive linear deflections of the ground surface are observed. These linear deformation features become more prominent over time with increasing lengths. The faults that produced these linear deformation patterns are known to be strata-bound to the DMG and the upper portions of the underlying shale strata. As discussed below, depletion of pore pressure from fluid production from shale strata and associated reservoir compaction is one mechanism that has been linked to the faulting at depth, and the development of linear patterns at the ground surface. Injection into the DMG is another mechanism that is linked to faulting. It has also been demonstrated that hydraulic fracturing in the Bone Spring and Wolfcamp shales has caused seismogenic rupture in some areas of the southern Delaware Basin (Skoumal et al., 2020; Savvaidis et al., 2020; Grigoratos et al., 2022).

Figs. 1a, 4d, 5d show that many of the published shallow faults have not hosted catalogued earthquakes and have therefore been slipping aseismically to produce the observed linear surface deformation patterns. The slip rate accelerated in 2019–21, and we conclude that seismic and aseismic rupture on the shallow faults in the southern Delaware Basin and the associated surface deflections arose from a complex combination of wastewater injection into the DMG, production of fluids from shale strata, and hydraulic fracturing of shale strata after 2010. However, fault displacement has accelerated since mid-2018 but seismicity has declined (Fig. 2), while ΔP_p in the DMG has continued to rise as the pace of injection has continued to increase or otherwise remain high. We also note that from mid-2018 onward, the rate of earthquakes in the southern Delaware Basin does not track any of the possible causal factors. One possibility is that hydraulic fracturing of shale strata may have played a role in triggering initial co-seismic slip on the deep extensions of the faults in the early phase of hydrocarbon development in the Delaware Basin (e.g., 2010 through mid-2018). In this hypothesis, hydraulic fracturing, with its hundreds to thousands of psi of net pore pressure and associated stress perturbation, might have served to overcome the natural cohesion along the shallow faults. The faults could then be kept active, principally aseismically, by subsidence from fluid production and pressurization from injection.

4.2. Uplift from injection

The observed uplift patterns closely coincide temporally and generally coincides spatially with shallow injection, as expected. The uplift comes from inflation of the DMG strata where injection is occurring and is associated with ΔP_p ranging from 0 up to ~3.5 MPa by the end of 2021. With ΔP_p of up to 3.5 MPa, we would expect to observe isolated

areas of uplift of up to 14 cm. However, we only observe up to 7 cm by the end of 2021, even in areas free of production. To explain this discrepancy, we propose that there has been a dynamic change in the behavior of the DMG reservoir as subject to ΔP_p from injection. This process begins with rupture of the most sensitive portions of the shallow fault system during hydraulic fracturing, ΔP_p in the DMG, and asymmetric subsidence from withdrawal of fluids from the shale strata. Once the faults became unstable, they could serve as permeable corridors allowing pore pressure to spread out laterally, acting, in essence, as conduits (Zhu et al., 2020). Across-fault permeability reduction caused by slip and juxtaposition of facies of contrasting permeability could further contribute to directional flow (e.g., Bense and Person, 2006). Transfer of ΔP_p from areas of concentrated injection in the more central areas of the basin to the northwest and southeast along the shallow faults as shown in Fig. 1a would underlie this mechanism. The pore pressure increase would preferentially follow the critically-stressed and active faults and diffuse into the host rock. Five observations combine to support this hypothesis (refer to Figs. 1a; 4d; 5d): (1) the development of a few cm of uplift to the west of U1-U3 is many km away from areas of injection and parallel to the trend of mapped faults and the interpreted surficial lineations; (2) uplift from inflation in the DMG to the west of U1-U3 is observed to terminate in spatial coincidence with the outcrop of the DMG along the western basin margin; (3) the evolution of linear features at the ground surface suggesting faulting in the DMG follows the azimuth of $S_{H\max}$; (4) patterns of earthquakes align with linear faulting; and (5) the analysis of fracture gradient shows that gradients are lower where induced faulting is prevalent. We interpret these five observations to support our hypothesis of fault valving and directional pore pressure migration.

We suggest that the spatiotemporal distribution of uplift we observe can be used to modify existing hydrogeologic models of ΔP_p evolution in the DMG to introduce anisotropic and stress-sensitive permeability, which could provide improvements in the models to forecast pore pressure and stress change in the reservoir.

We see no evidence of uplift from deep injection in the northern Delaware Basin where the footprint of deep injection does not coincide with areas of uplift. This outcome is expected as the strata used for this deep injection are dominated by geomechanically stiff carbonates with permeability systems are dominated by karst, fractures, and faults (Smye et al., 2022). These strata are at a minimum of 2.2 km below sea level where it is targeted for injection in our study area.

4.3. Relationship to prior publications

Several recent papers reported analysis of InSAR surface deformation observations associated with fluid withdrawal and wastewater injection in the Permian Basin (Hennings et al., 2021; Zhai et al., 2021; Horne et al., 2022; Staniewicz et al., 2020; Pepin et al., 2022; Deng et al., 2020; Dvory et al., 2022; Patton, 2023). Here, our work presents the most comprehensive InSAR analysis over a period of 7 years (2015–21) that coincided with a massive volume increase of oil production and wastewater injection in the Delaware Basin. Compared to the most recent InSAR works in West Texas (Staniewicz et al., 2020; Pepin et al., 2022), our results reveal rapidly accelerating surface deformation signatures that occurred over a much broader region with greater rates. Our study shows that the summation of dynamic loading from fluid production and injection at all levels of strata needs to be considered to gain a quantitative understanding of stress change on faults and mechanisms of rupture. Employing coupled modeling of diffusion with rate-state frictional response provides an assessment of the magnitude of ΔP_p required to cause both initial rupture of shallow faults and ongoing aseismic slip (Dvory et al., 2022). This work also highlights the complexity involved in quantitatively parameterizing the faulted injection aquifer to replicate rupture behavior mechanistically.

An important contribution of this paper is that we provide an assessment of surface deformation in the Delaware Basin as a geologic

entity using multiple temporal windows. We dissect the response of the basin into regions where we investigate the drivers locally. We show how the ground surface displacement has changed laterally, vertically, and temporally. We find that subsidence is concentrated directly above strata subject to production but the patterns of uplift from injection are more diffuse and complex, and we discuss how fault systems are evolving as activated principally by injection and modified by production. Using multiple lines of evidence, we conclude that faulting from injection produces a directional or valving response that produces lateral anisotropic pore pressure diffusion and uplift. We conclude that the Delaware Basin is geomechanically sensitive across multiple scales and processes.

4.4. Applications for sustainable development

Understanding the spatiotemporal patterns of subsidence from hydrocarbon production could be valuable in the development of reservoir response models that could aid in optimization of horizontal well spacing, stacking, and sequencing. Future studies should consider the depth, reservoir character, and fluid composition as they spatiotemporally relate to subsidence. These models could also be used to understand the ratios and mobility of reservoir fluids (oil, gas, water) in effort to forecast future water-handling requirements.

Understanding the distribution of dynamic change to the DMG and overlying units due to shallow injection is a more pressing concern. In an effort to mitigate the currently observed earthquakes in the northern Delaware Basin as induced by deep injection, many operators of deep injection wells are currently reorienting their operations to target the (shallow) DMG for injection. Due to regulatory limitations of wastewater injection in New Mexico, at least 320,000 m³ (2 million barrels) of wastewater per day are currently transported across the state line into Texas (Patton, 2023) and injected into the DMG, which contributes to the uplift of region U6. Estimates of future wastewater injection in the Delaware Basin over the next ~25 years range as high as 400 million m³ in addition to the ~210 million m³ injected thus far. Our ΔP_p model and InSAR analysis shows that DMG pore pressure increase, and reservoir inflation is already widespread in the Texas portion of the Delaware Basin. In the southern Delaware Basin, shallow injection has caused widespread fault reactivation and directional pore pressure diffusion. Although earthquakes have been induced at shallow levels, fault valving and far-field diffusion of pore pressure may be beneficial, at least temporarily, in facilitating dissipation of local concentrations of pore pressure and DMG reservoir inflation, which could otherwise challenge the integrity of the sealing overburden and existing wellbores. We recommend quantitative study of response of the DMG and its overburden to injection to assess the controls on dynamic reservoir evolution and the integrity of the overburden to both hydraulic fracturing and faulting due to injection and ΔP_p . This type of analysis can be used to assist with planning for future injection to utilize the DMG to the best benefit on a regional basis.

There are now approximately 65,000 production and injection wellbores that have been completed in the Delaware Basin since drilling began in the 1920s. Of those, there are ~27,000 active, inactive, and abandoned petroleum wells in the basin which were completed prior to the onset of shale development in 2009. We know of no compromise to wellbores to date in the Delaware Basin proper that have resulted in fouling of groundwater but the occurrence of wells leaking at the surface is increasing. There have been several well-documented cases of compromised wellbores with geysers of fluid to the east on the Central Basin Platform (Kim et al., 2018; Kim and Lu, 2018; Gold, 2022a, 2022b). The geomechanical ability of the evaporite-rich overburden relied upon to seal injected wastewater from groundwater supplies must have limits and regional variations which should be understood. Ground surface movements both up and down, faulting with deflections reaching the ground surface, and induced earthquakes are all indications that the Delaware Basin subsurface is geomechanically sensitive to

petroleum operations, the consequences of which should be understood to the best of our ability to mitigate associated hazards and shepherd sustainable development of the basin.

Funding

Center for Injection and Seismicity Research (CISR) and its industrial affiliates at The University of Texas at Austin, Bureau of Economic Geology (PH, KS, EH, JG, JPN, BS, RR).

NASA Earth Surface and Interior Program, Grant 80NSSC18K0467 (JC, SS).

CRediT authorship contribution statement

Conceptualization: PH, SS, KS, JC.
 Methodology: PH, SS, KS, JC.
 Investigation: PH, SS, KS, JG, JPN.
 Visualization: PH, SS, KS.
 Supervision: PH, JC.
 Writing – original draft: PH, SS, JC.
 Writing – review & editing: JC, KS, LH, JPN, BS.

Declaration of competing interest

The authors declare that they have no known competing financial interests or personal relationships that could have appeared to influence the work reported in this paper.

Data availability

Data used to prepare the maps for all figures presented are [*will be upon acceptance*] available as ArcMap shapefiles at: doi:<https://doi.org/10.18738/T8/LC31IZ>. This data includes InSAR ground surface displacements, injection data, production data, fault lines, For injection analytics, we use the B3 Insight database, which sources public data (<https://www.b3insight.com/>). Sentinel-1 single look complex (SLC) images can be accessed from the Alaska Satellite Facility (ASF) DAAC (<https://search.asf.alaska.edu>). GPS data were provided by the Texas Department of Transportation and processed by the Nevada Geodetic Laboratory (<http://geodesy.unr.edu>). For hydraulic fracture data we use the Frac Focus database, which sources public data (<https://fracfocus.org>). For oilfield production data we use S&P Ener-deq™, which sources public data (<https://ihsmarkit.com/products/oil-gas-tools-enerdeq-browser.html>). Earthquake data for Texas is available from the TexNet Earthquake Catalog at: <https://catalog.texnet.beg.utexas.edu/>. Relocated earthquake data (high resolution data) for the Texas part of the Delaware Basin is available at: <https://hirescatalog.texnet.beg.utexas.edu/> and information about the GrowClus software used to produce the high resolution earthquake data can be found at: <https://github.com/dttrugman/GrowClust/>. Earthquake data for New Mexico is available at: <https://geoinfo.nmt.edu/nmtdso/events/home.cfm>. Injection well test data for Texas can be obtained from the RRC at: <https://www.rrc.texas.gov/resource-center/data-visualization/oil-gas-data-visualization/drilling-permits/>. Data on groundwater from the Texas Ground Water Development Board Groundwater Database is available at: <https://www.twdb.texas.gov/groundwater/data/gwdb rpt.asp>. Information on orphaned wells from the Environmental Defense Fund (EDF) is available at: <https://www.edf.org/search/content?keys=orphaned%20wells%20texas>. The RRC Orphaned Well Plugging Program and data is available at: <https://www.rrc.texas.gov/news/010323-federal-well-plugging-data-visualization/> and the well plugging priority criteria is available at: <https://www.rrc.texas.gov/media/3hjhjroj/well-plugging-prioritization.pdf>. All other data presented is available in the supplement.

Acknowledgments

We thank B3 for access to injection data, S&P for access to their Enerdeq database and Petra software, Computer Modeling Group (CMG) for access to their STARS and GEM softwares, and to Schlumberger for access to their Petrel software.

Appendix A. Supplementary data

Supplementary data to this article can be found online at <https://doi.org/10.1016/j.scitotenv.2023.166367>.

References

- Bense, V.F., Person, M.A., 2006. Faults as conduit-barrier systems to fluid flow in siliciclastic sedimentary aquifers. *Water Resour. Res.* 42, W05421. <https://doi.org/10.1029/2005WR004480>.
- Berardino, P., Fornaro, G., Lanari, R., Sansosti, E., 2002. A new algorithm for surface deformation monitoring based on small baseline differential SAR interferograms. *IEEE Trans. Geosci. Remote Sens.* 40 (11), 2375–2383. Nov. 2002. <https://doi.org/10.1109/TGRS.2002.803792>.
- Blewitt, G., Hammond, W., Kreemer, C., 2018. Harnessing the GPS data explosion for interdisciplinary science. *EOS* 99, 1–2. <https://doi.org/10.1029/2018EO104623>.
- Chen, C.W., Zebker, H.A., 2001. Two-dimensional phase unwrapping with use of statistical T60 models for cost functions in nonlinear optimization. *J. Opt. Soc. Am. A* 18 (2), 338–351.
- Cleveland, W.S., 1979. Robust locally weighted regression and smoothing scatterplots. *J. Am. Stat. Assoc.* 74 (368), 829–836.
- Deng, F., Dixon, T.H., Xie, S., 2020. Surface deformation and induced seismicity due to fluid injection and oil and gas extraction in western Texas. *J. Geophys. Res. Solid Earth* 125. <https://doi.org/10.1029/2019JB018962> e2019JB018962.
- Dvory, N.Z., Zoback, M.D., 2021a. Assessing fault slip potential in a continuously varying stress field—Application in the Delaware Basin. In: 55th US Rock Mechanics/Geomechanics Symposium. American Rock Mechanics Association.
- Dvory, N.Z., Zoback, M.D., 2021b. Prior oil and gas production can limit the occurrence of injection-induced seismicity: A case study in the Delaware Basin of western Texas and southeastern New Mexico, USA. *Geology* 49. <https://doi.org/10.1130/G49015.1>.
- Dvory, N.Z., Yang, Y., Dunham, E.M., 2022. Models of injection induced aseismic slip on height-bounded faults in the Delaware Basin constrain fault-zone pore pressure changes and permeability. *Geophys. Res. Lett.* 49 <https://doi.org/10.1029/2021GL097330> e2021GL097330.
- Emardson, T.R., Simons, M., Webb, F.H., 2003. Neutral atmospheric delay in interferometric synthetic aperture radar applications: statistical description and mitigation. *J. Geophys. Res. Solid Earth* 108 (B5), 1–8.
- Ewing, T.E., 2019. Tectonics of the West Texas (Permian) basin—Origins, structural geology, subsidence, and later modification. In: Ruppel, S.C. (Ed.), Anatomy of a Paleozoic Basin: The Permian Basin, USA (Vol. 1, Ch. 4). The University of Texas at Austin, Bureau of Economic Geology Report of Investigations 285, pp. 63–96. AAPG Memoir 118.
- Ferratti, A., Prati, C., Rocca, F., 2001. Permanent scatterers in SAR interferometry. *IEEE Trans. Geosci. Remote Sens.* 39 (1), 8–20.
- Frohlich, C., Hayward, C., Rosenblit, J., Aiken, C., Hennings, P., Savvaidis, A., Lemons, C., Horne, E., Walter, J.I.J.I., DeShon, H.R.H.R., 2020. Onset and cause of increased seismic activity near Pecos, West Texas, United States, from observations at the Lajitas TXAR seismic array. *J. Geophys. Res. Solid Earth* 125.
- Galloway, D.L., Jones, D.R., Ingebretsen, S.E., 1999. Land subsidence in the United States. *U.S. Geol. Surv. Cir.* 1182, 177.
- GAT (Geologic Atlas of Texas) (2014). Bureau of Economic Geology, <https://store.beg.utexas.edu/25-geologic-atlas-of-texas>.
- Ge, J., Nicot, J.-P., Hennings, P.H., Smyre, K.M., Hosseini, S.A., Gao, R.S., Breton, C.L., 2022. Recent water disposal and pore-pressure evolution in the Delaware Mountain group, Delaware basin, Southeast New Mexico and West Texas, USA. *J. Hydrol.* 40 <https://doi.org/10.1016/j.ejrh.2022.101041>.
- Gold, R. (2022a). Texas Monthly, <https://www.texasmonthly.com/news-politics/mystery-west-texas-geyser-deepens/>.
- Gold, R. (2022b). Texas Monthly, <https://www.texasmonthly.com/news-politics/ashley-watt-rancher-chevron-toxic-water/>.
- Grigoratos, I., Savvaidis, A., Rathje, E., 2022. Distinguishing the causal factors of induced seismicity in the Delaware Basin: hydraulic fracturing or wastewater disposal? *Seismol. Res. Lett.* 93 (5), 2640–2658. <https://doi.org/10.1785/0220210320>.
- Hennings, P., Allwardt, P., Paul, P., and others (2012). Relationship between fractures, fault zones, stress and reservoir productivity in the suban gas field, Sumatra, Indonesia, AAPG Bull., v. 96, p. 753–772, doi:<https://doi.org/10.1306/08161109084>.
- Hennings, P.H., Dvory, N., Horne, E.A., Li, P., Savvaidis, A., Zoback, M., 2021. Stability of the fault systems that host induced earthquakes in the Delaware Basin of West Texas and Southeast New Mexico. *Seismol. Rec.* 1 (2), 96–106.
- Horne, E.A., Hennings, P.H., Zahm, C.K., 2021. Basement structure of the Delaware basin. In: Callahan, O.A., Eichhubl, P. (Eds.), The Geologic Basement of Texas: A Volume in Honor of Peter Flawn. The University of Texas at Austin, Bureau of Economic Geology Report of Investigations, Austin, Texas.

- Horne, E., Hennings, P., Smye, K., Staniewicz, S., Chen, J., Savvaidis, A., 2022. Structural characteristics of shallow-normal faults in the Delaware Basin, Texas and New Mexico. Interpretation. <https://doi.org/10.1190/int-2022-0005.1>.
- Huang, G., Horne, E., Kavoura, F., Savvaidis, A., 2022. Characteristics of seismogenic structures and 3D stress state of the Delaware Basin of West Texas as constrained by earthquake source mechanisms. *Seismol. Res. Lett.* XX 1–10. <https://doi.org/10.1785/0220220054>.
- Kim, J.-W., Lu, Z., 2018. Association between localized geohazards in West Texas and human activities, recognized by Sentinel-1A/B satellite radar imagery. *Sci. Rep.* 8 (4727) <https://doi.org/10.1038/s41598-018-23143-6>.
- Kim, J.-W., Zhong, Lu, Kaufmann, J., 2018. Evolution of sinkholes over winkle, Texas, observed by high-resolution optical and SAR imagery. *Remote Sens. Environ.* <https://doi.org/10.1016/j.rse.2018.12.028>.
- Lemons, C.R., McDaid, G., Smye, K.M., Acevedo, J.P., Hennings, P.H., Banerji, D.A., Scanlon, B.R., 2019. Spatiotemporal and stratigraphic trends in salt-water disposal practices of the Permian Basin, Texas and New Mexico, United States. *Environ. Geosci.* 26, 107–124.
- Maghsoudi, Y., Hooper, A.J., Wright, T.J., Lazecky, M., Ansari, H., 2022. Characterizing and correcting phase biases in short-term, multilooked interferograms. *Remote Sens. Environ.* 275, 113022.
- NMITSO (New Mexico Tech Seismological Observatory, 2021), Seismic Events — New Mexico Tech Seismological Observatory, //geoinfo.nmt.edu/nmitso/events/home.cfm. Accessed September 1, 2022.
- Patton, P. (2023). Texas is giving away revenue and taking New Mexico's waste, Dallas Morning News Opinion, <https://www.dallasnews.com/opinion/commentary/2023/01/21/texas-is-giving-away-revenue-and-taking-new-mexicos-waste/?outputType=amp>.
- Pepin, K.S., Ellsworth, W.L., Sheng, Y., Zebker, H.A., 2022. Shallow aseismic slip in the Delaware Basin determined by Sentinel-1 InSAR. *J. Geophys. Res. Solid Earth* 127. <https://doi.org/10.1029/2021JB023157>.
- Reedy, R. C. and Scanlon, B.R. (2022). Water Use by the Mining Industry of Texas, Final Contract Report for the Texas Water Development Board, 78 p.
- Savvaidis, A., Lomax, A., Breton, C., 2020. Induced seismicity in the Delaware Basin, West Texas, is caused by hydraulic fracturing and wastewater disposal. *Bull. Seismol. Soc. Am.* 110 (5), 2225–2241.
- Scanlon, B.R., Ikonnikova, S., Yang, Q., Reedy, R.C., 2020. Will water issues constrain oil and gas production in the United States? *Environ. Sci. Technol.* 54 (6), 3510–3519. <https://doi.org/10.1021/acs.est.9b06390>.
- Segall, P., 1992. Induced stresses due to fluid extraction from axisymmetric reservoirs. *Pure Appl. Geophys.* 139 (3–4), 535–560.
- Sheng, Y., Pepin, K.S., Ellsworth, W.L., 2022. On the depth of earthquakes in the Delaware Basin: a case study along the Reeves–Pecos county line. *Seismol. Rec.* 2 (1), 29–37.
- Skoumal, R.J., Barbour, A.J., Brudzinski, M.R., Langenkamp, T., Kaven, J.O., 2020. Induced seismicity in the Delaware Basin, Texas. *J. Geophys. Res.* 125 (1) <https://doi.org/10.1029/2019JB018558>.
- Smye, K., Hennings, P., Nicot, J.-P., 2022. Role of Geology in Induced Seismicity Associated with Shallow and Deep Wastewater Injection. AGU Annual Meeting, Chicago.
- Smye, K., Banerji, D.A., Eastwood, R., McDaid, G., Hennings, P., 2021. Lithology and reservoir properties of the Delaware Mountain Group of the Delaware Basin and implications for saltwater disposal and induced seismicity. *J. Sediment. Res.* 91, 1113–1132.
- Staniewicz, S., Chen, J., Lee, H., Olson, J., Savvaidis, A., Reedy, R., Breton, C., Rathje, E., Hennings, P., 2020. InSAR reveals complex surface deformation patterns over an 80,000 km² oil-producing region in the Permian Basin. *Geophys. Res. Lett.* 47.
- Teatini, P., Gambolati, G., Ferronato, M., Settari, A., Walters, D., 2011. Land uplift due to subsurface fluid injection. *J. Geodyn.* 51 (1), 1–16.
- TexNet, (2021). "TexNet Earthquake Catalog": Bureau of Economic Geology, <https://www.beg.utexas.edu/texnet-cisr/texnet/earthquake-catalog>. Accessed September 1, 2022.
- TexNet, (2022). "TexNet Hi-Res Earthquake Catalog": Bureau of Economic Geology, doi:10.15781/76hj-ed46. Accessed September 1, 2022.
- Townend, J., Zoback, M.D., 2000. How faulting keeps the crust strong. *Geology.* [https://doi.org/10.1130/0091-7613\(2000\)28%3C399:HFKTCS%3E2.0.CO;2](https://doi.org/10.1130/0091-7613(2000)28%3C399:HFKTCS%3E2.0.CO;2).
- TPWC (Texas Produced Water Consortium, 2022), Beneficial use of produced water in Texas: challenges, opportunities and the path forward, Texas Produced Water Consortium Report to the Texas Legislature 2022, 130 p.
- Yunjun, Z., Fattah, H., Amelung, F., 2019. Small baseline InSAR time series analysis: unwrapping error correction and noise reduction. *Comput. Geosci.* 133, 104331.
- Zebker, H., 2021. Accuracy of a model-free algorithm for temporal InSAR tropospheric correction. *Remote Sens.* 13 (3), 409.
- Zhai, G., Shirzaei, M., Manga, M., 2021. Widespread deep seismicity in the Delaware Basin, Texas, is mainly driven by shallow wastewater injection. *Proc. Natl. Acad. Sci.* 118 (20) <https://doi.org/10.1073/pnas.2102338118>.
- Zhang, J., Yin, S.-X., 2017. Fracture gradient prediction: an overview and an improved method. *Pet. Sci.* 14, 720–730. <https://doi.org/10.1007/s12182-017-0182-1>.
- Zheng, Y., Zebker, H.A., 2017. Phase correction of single-look complex radar images for 894 user-friendly efficient interferogram formation. *IEEE J. Select Topic Appl. Earth Observ. Remote Sens.* 10 (6), 2694–2701. <https://doi.org/10.1109/JSTARS.2017.2697861>.
- Zheng, Y., Fattah, H., Agram, P., Simons, M., Rosen, P., 2022. On closure phase and systematic bias in multilooked SAR interferometry. *IEEE Trans. Geosci. Remote Sens.* 60, 1–11.
- Zhu, W., Allison, K.L., Dunham, E.M., 2020. Fault valving and pore pressure evolution in simulations of earthquake sequences and aseismic slip. *Nat. Commun.* 11, 4833. <https://doi.org/10.1038/s41467-020-18598-z>.